Metals and Materials International (2023) 29:591–606
https://doi.org/10.1007/s12540-022-01260-2

Carrying Gas Influence and Fabrication Parameters Impact in 3D Manufacturing of In Situ TiN-Ti Composites by Direct Laser Deposition

C. Sánchez de Rojas Candela[1] · A. Riquelme[1] · P. Rodrigo[1] · J. Rams[1]

Received: 6 January 2022 / Accepted: 7 June 2022 / Published online: 5 July 2022

Abstract
The difficulty of getting a correct distribution of the reinforcement in the metal matrix and the complexity for achieving a good-metallurgy matrix-reinforcement bonding has limited the development of additive manufacturing of metal matrix composites. This research proposes the use of a reactive atmosphere during the fabrication process to obtain titanium matrix composites reinforced with TiN. The relation between the carrying gas and the process parameters used with the presence of porous and defects, the microstructure, and microhardness has been obtained. Nitrogen was used as the carrying gas of the titanium powder. Under laser irradiation, the particles melt and react with nitrogen, resulting in the formation of a titanium matrix composite highly reinforced with TiN. The composite obtained had a microhardness increase between 50 and 100% in comparison with titanium samples fabricated in the same conditions in an argon atmosphere. Three reaction mechanisms have been proposed to take place in the microstructure, depending on the amount of nitrogen in the titanium particles, and its diffusion in them during the manufacture.

Keywords Direct laser deposition · Titanium nitride · In situ reaction · Metal matrix composite

1 Introduction

Additive manufacturing (AM) is a 3D printing fabrication method in which parts are built layer by layer by depositing material according to a CAD design [1]. It is possible to use a wide range of materials such as metals, ceramics, polymers, and composites, although adjusting some materials to this technology is a challenge. The final quality and finishing are largely determined by the material used. Since homogeneous materials do not always provide the best mechanical properties, metal matrix composites (MMCs) reinforced with different materials are being widely studied because they combine the properties of two different types of materials, resulting in new materials of high interest in many applications [2]. AM technology provides the possibility of creating metal matrix composites with numerous advantages, such as design flexibility, process modeling and control, and almost no waste of material [3]. However, it is quite complicated to fabricate MMCs by this technique and further research needs to be done.

Direct Laser Deposition (DLD) is one of the most used AM methods for metal parts. In it, the material is deposited layer by layer by melting a metal powder or a wire with a laser [4–7]. The selected fabrication parameters are key in this process and determine the properties of the resulting material. This is caused by the high temperatures reached, which form a melt pool and a Heat Affected Zone (HAZ) during the process; the shape and dimensions of these zones depend on the selected manufacturing parameters [8]. Laser scanning speed and laser power are the DLD process parameters that most affect the microstructural, mechanical, and morphological properties of the final composite material [9]. These fabrication parameters define the re-melting of the previous layer, the cooling rates, and the grain size [10].

DLD technology allows altering the atmosphere used for the fabrication process. Argon is usually used as inert gas to carry the materials in powder form and protect them from being oxidized. Recently, a different approach tested showed that the gas in the DLD can be partially substituted by a reactive gas such as nitrogen [11]. Nitrogen can react with the metal matrix and form in-situ reinforcement compounds, which leads to the creation of composite materials with

✉ A. Riquelme
ainhoa.riquelme.aguado@urjc.es

[1] Materials Science and Engineering Group, Universidad Rey Juan Carlos, Madrid 28933, Spain

improved properties such as high hardness and wear resistance [12]. Therefore, the reactive atmosphere influences the composition and properties of the fabricated materials [13].

Titanium alloys have been used in numerous applications for many years, ranging from transport to medical industries. Recently, additive manufacturing has driven the fabrication and use of titanium alloy parts reducing costs and manufacturing time [14]. The raw materials used in AM entail a higher cost than those utilized in traditional techniques, but the average price per manufactured part by AM is reduced as less material and manufacturing processes are used [15]. In particular, Ti6Al4V is one of the most utilized titanium alloys in conventional fabrication and lately in AM [5, 16]. Ti6Al4V is an alpha–beta alloy that is used in the manufacture of aerospace components and biomedical prostheses due to its great resistance to corrosion, high biocompatibility and osseointegration, and lightweight [17, 18]. Furthermore, Ti6Al4V has high fatigue resistance, good structural stability, and a high elastic limit. However, its limited wear resistance is the main drawback of this alloy, especially when it is used for applications like hip implants, which leads to a material deterioration where abrasive particles are detached from the protheses and provoke inflammation and pain with the consequent implant failure [19]. Titanium matrix composites (TMCs) based on Ti6Al4V reinforced with ceramic particles could potentially replace non-reinforced alloys as they show improved hardness and wear behavior [20, 21].

The weakest characteristic of ceramic reinforced metal matrix composites is the interaction between matrix and reinforcement. If it is not very high, under certain wear conditions the ceramic particles could detach from the metal matrix, reducing the wear resistance [22]. This predominately occurs when the reinforcement material is introduced in an ex-situ configuration, where is more difficult to create a good interfacial bonding with the metal matrix [23]. However, this is not the case with in-situ reinforcement, since the reinforcing phases are formed from the molten metal matrix and, therefore, the matrix-reinforcement interaction is well established.

The manufacture of Ti6Al4V samples is complex because of the high melting temperature of this alloy. Furthermore, the fabrication of TMCs is even more difficult as the adequate mixing of the particles and the ceramic reinforcement in the liquid state is conditioned by the temperature required and the reactivity of the alloy [24]. Surprisingly, the use of AM for Ti alloys has simplified the manufacture of complex pieces as this material adapts well to AM because of its limited thermal conductivity and the possibility of controlling the atmosphere. Therefore, the use of AM to TMCs would allow the manufacture of pieces with improved mechanical properties and with manufacturing flexibility that is unmatched with casting processes and with reduced costs and wastes compared to machining [25].

The addition of reinforcements in titanium matrixes such as TiN improves the wear behavior of the material due to its different properties related to its dendritic microstructures. In 2015, P. Rodrigo et al. [26] developed a patent to manufacture in situ Ti-TiN composites coatings by laser cladding. Subsequent research work has been performed to reinforce coatings made of Ti6Al4V with in-situ TiN. B. Shi et al. [27] prepared TiN reinforced composite coatings on Ti6Al4V by using plasma spray technique with nitrogen as carrying gas, which resulted in a greater microhardness and abrasive resistance of the material. In the same way, C. Shong et al. [28] used a plasma spray to fabricate in-situ TiN coatings on Ti6Al4V that significantly enhanced the mechanical properties of the titanium alloy. X. Zhao et al. [29] formed a coating reinforced in-situ with TiN on a Ti-Nb-Zr-Ti alloy through laser radiation. They concluded that both wear and corrosion resistance improved after laser texturing in N_2. Furthermore, in-situ ceramic reinforced titanium matrix composites (TMCs) have been studied. K.D. Traxel et al. [30] developed pure titanium composites with a 5 wt% of in-situ $B_4C + BN$ reinforcement by laser-based AM, which resulted in superior yield strength and wear resistance due to the formation of in-situ reinforcement phases. W. Wei et al. [31] processed in-situ synthesized TiN and AlN reinforced Ti6Al4V matrix composites by the gas–liquid reaction in nitrogen atmospheres with selective laser melting techniques; microhardness, compressive yield strength, and ultimate compressive strength increased with the nitrogen concentration.

Nevertheless, the works indicated before use the in-situ nitriding of the Ti6Al4V alloy in Laser Powder Bed Fusion (L-PBF) fabrication. In this technique, the powder is firstly deposited layer by layer and then the selected zones are molten by the laser, and they carried out this process in a nitrogen-rich atmosphere. The thickness of the layers in this technique range between 50 μm to 150 μm and the particles are in a static state. This technique provides highly detailed samples, while their size is limited by that of the powder bed size. In this work, we have used the Direct Laser Deposition (DLD) technique, in which the particles are carried by a gas that sprays them while they are heated and molten by a laser. The layer thickness is much greater as it can reach about 1 mm and the particles are moving inside the gas before being deposited in the sample. This technique cannot be used to manufacture highly detailed structures, but very large samples can be manufactured as there is no limitation associated with a powder bed. Due to the differences shown before, the number of defects, microstructure, and mechanical and corrosion properties differ from one another as has been shown in comparative works on other materials [16], so the results from L-PBF cannot be extended to other additive manufacturing techniques.

In this research, a novel and promising methodology to create TMCs has been studied. Ti6Al4V / TiN composites have been fabricated by Direct Laser Deposition-Additive Manufacturing by substituting argon for nitrogen as the carrying gas, which led to the formation of in-situ titanium nitride reinforcement in the Ti6Al4V matrix. Two different conditions for both the laser power and the scanning speed have been analyzed (650 and 1200 W, and 5 and 10 mm/s, respectively). The comparison with unreinforced materials manufactured with inert argon as carrying gas shows an improvement in mechanical properties such as microhardness. The influence of the carrying gas and the fabrication parameters in the morphology, porosity, and microstructure of the manufactured parts has been determined and possible reaction mechanisms are proposed for the formation of the composite material.

2 Experimental Procedure

Thin wall samples (length = 60 mm and height = 15 mm) of unreinforced Ti6Al4V and in-situ reinforced Ti6Al4V/TiN composites were manufactured by DLD using 316L sheets (100 × 100 × 20 mm) as support material. Figure 1a shows the spherical morphology of the Ti6Al4V commercial powder used and the powder characteristics are detailed in Table 1. Figure 1b shows the powder particle size distribution determined with SemAfore image analysis software. The particles have different diameters and the larger number of particles are in between 9 and 21 µm.

The laser used was a high-power diode laser (1300 W) (ROFIN DL013S) with a wavelength between 808 and 940 nm. The metallic powder was maintained at room temperature and was sprayed coaxially with the laser beam through a Fraunhofer IWS COAX 8 coaxial nozzle. The effect of the carrying gas was analyzed using argon or nitrogen (4.5 atm pressure and 0.05 L s^{-1} flow rate). The powder and the laser focus were 12.5 mm below the nozzle tip. The powder feed ratio was 5 g/min and the laser focus overlapped with the powder focus. In addition, this system is placed in an ABB IRB2400 robot that moves the DLD system (powder nozzle and laser) with the programmed manufacturing conditions. A hot plate connected to a temperature control system was used as substrate support. It was set to 250 °C for all manufacturing conditions. The effect of the laser power and the laser scanning speed has been analyzed. Table 2 shows the set of samples manufactured with their corresponding fabrication conditions.

A critical parameter for the build-up of the pieces is the layer height. It has not been forced to be the same for every manufacturing condition as the efficiency of the process depends on the other manufacturing parameters. To optimize the height increase per layer for each laser parameter used, a single layer (length = 60 mm) of each condition was built before the thin wall fabrication (Fig. 2a). These single layer heights were measured using a caliper with a precision of ± 0.01 mm, and these values determined the height increase per layer for the manufacturing. Thin wall samples (length = 60 mm) of Ti6Al4V were built using the parameters shown in Table 2. The schematic representation of the DLD fabrication process is shown in Fig. 2b. The wall height was fixed at 15 mm. The number of layers depended on the

Table 1 Powder properties

Product	Supplier	D10 (µm)	D50 (µm)	D90 (µm)	ρ (g cm^{-3})
Ti6Al4V	Renishaw	11.88	20.33	35.90	4.42

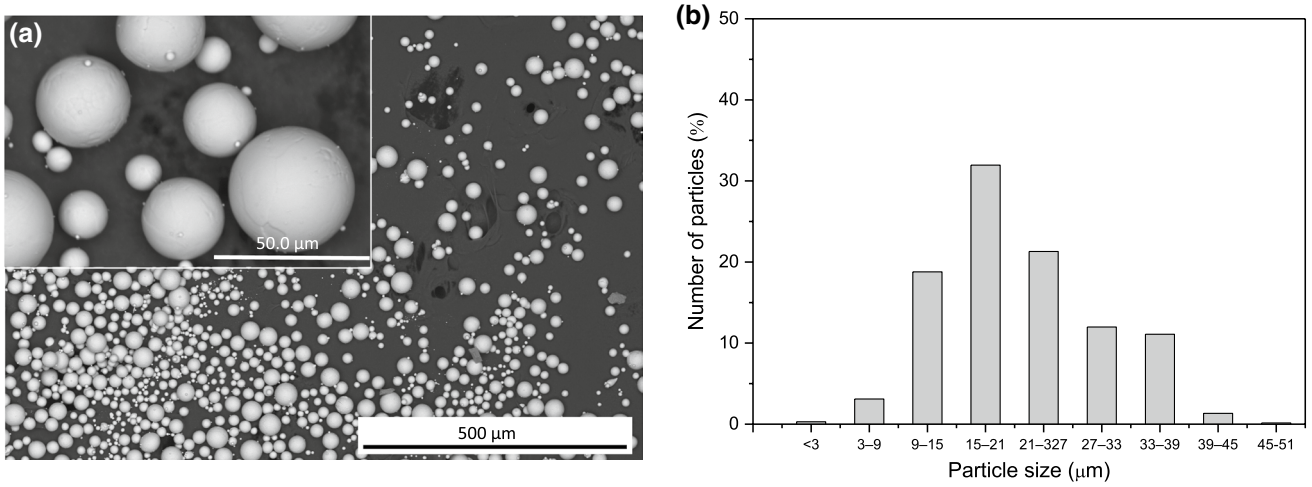

Fig. 1 **a** Feed powder used during the DLD additive manufacturing process, inset detail of the powder showed in **a**; **b** particle size distribution of the Ti6Al4V powder

Table 2 Set of experimental conditions used in this work

Condition	Initial laser power (W)	Final laser power (W)	Scanning speed (mm/s)	Carrying gas	Abbreviated name
C1	650	100	5	Argon	650-5-Ar
C2	650	100	10	Argon	650-10-Ar
C3	1200	700	5	Argon	1200-5-Ar
C4	1200	700	10	Argon	1200-10-Ar
C5	650	100	5	Nitrogen	650-5-N
C6	650	100	10	Nitrogen	650-10-N
C7	1200	700	5	Nitrogen	1200-5-N
C8	1200	700	10	Nitrogen	1200-10-N

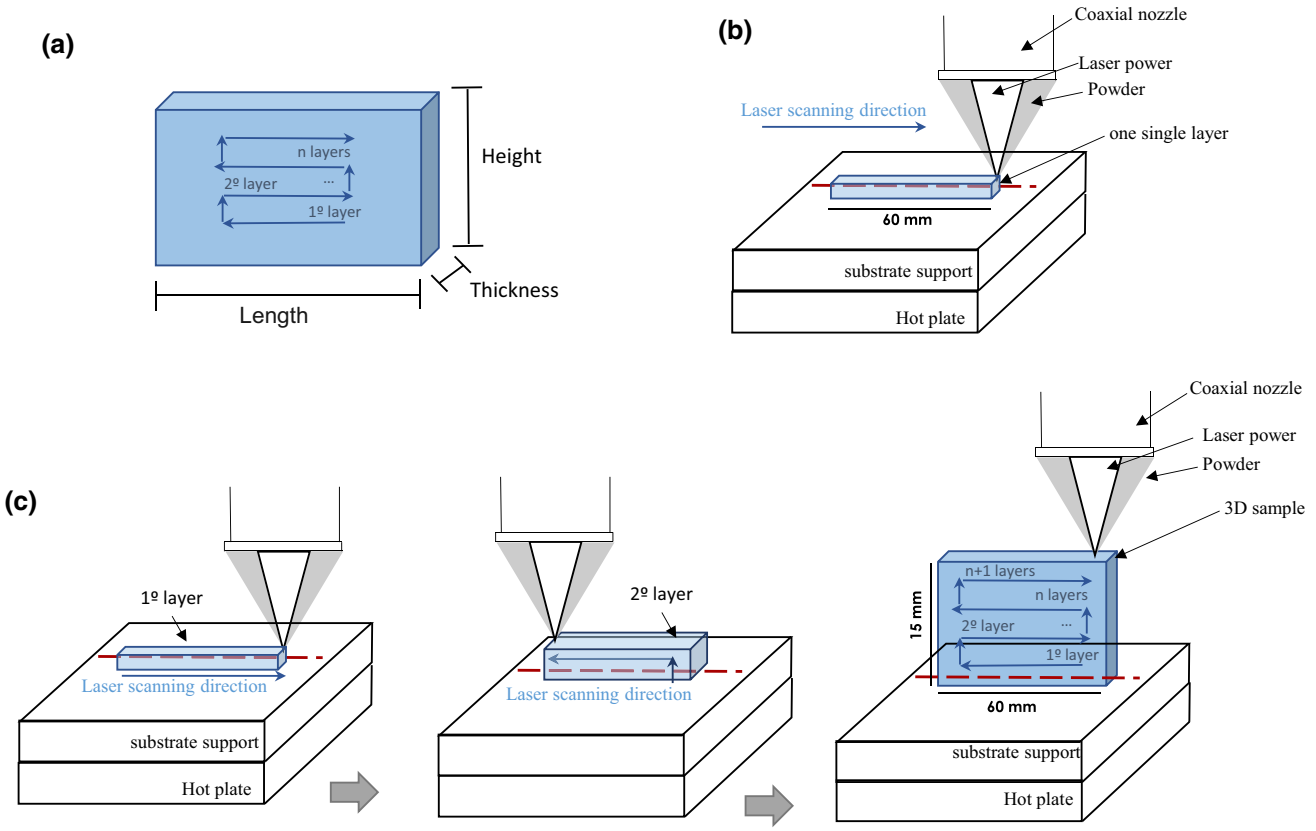

Fig. 2 **a** Schematic DLD sample design; **b** schematic representation of the set-up DLD fabrication process of a single layer; **c** schematic representation of multilayer DLD manufacturing

height increment per layer, which was determined for the different scanning speeds and carrying gas.

Some tests were performed at different laser powers to optimize the manufacturing parameters. Laser power values below 300 W could not melt the titanium particles. At the laser power value of 650 W, a high-quality first layer was deposited but maintaining this value in the following layers for the lower laser scanning speed led to the melting of the manufactured samples. Thus, the laser power was gradually reduced during the deposition process from the first to the last layer to avoid excessive heat input. The power input depended on the difference between the initial and the final laser power and the scanning speed (Table 2).

The two manufacturing ranges were possible because the shape and size of the layers differed and because the parameters were adapted for each condition. The samples manufactured with 1200 W were thicker, what allowed transferring more heat to the substrates. Also, the layers were higher, so there was more material to absorb the heat

of the laser and the total number of laser passes needed to reach the specified height was smaller.

Regarding the scanning speed, two different values were selected, 5 and 10 mm/s. These laser scanning speeds are rather slow so that the energy density was enough to melt the titanium particles and far enough apart to be compared.

Samples were metallography prepared for analyzing its microhardness and its microstructure profile. The cross-sections of the samples were cut, mounted in an electrically conductive resin, wet grounded using a sequence of abrasive silicon carbide (400 to 4000 grit), and finally polished using a 1 µm diamond solution and ethylene glycol as lubricant.

The dimensions of the cross-sections (height and width) were measured with an image analysis software (Leica Application Suite) on the captured images obtained with a light optical microscope (OM; Leica DMR). The porosity percentages were also quantified with Leica Application Suite on a total of five different optical microscopy images taken at low magnifications to capture a representative area of the porosity levels. Microstructures were evaluated with image analysis software on the optical microscopy images and also on images obtained with a scanning electron microscope (SEM; Hitachi S-3400 N), equipped with an energy dispersive X-ray spectrometer (EDX). X-ray diffraction (XRD) was performed with a Panalytical X'Pert PRO diffractometer and analyzed with X'Pert HighScore Plus software. The radiation source was Cu Kα ($\lambda = 1.5406$ Å) operating at 45 kV and 300 mA. The 2θ scanning range was from 20° to 95° with a step of 0.02° and an acquisition time of 20 s.

Vickers microhardness ($HV_{0.1,}$ and 15 s) values were measured by using a Shimadzu microhardness tester on the cross-section of the specimens. The microhardness measurements were performed from the substrate to the top of the sample with distances of 1000 µm between the indentations.

3 Results and discussion

An image of a fabricated part by DLD additive manufacturing is shown in Fig. 3a. The thin wall-like morphology of the sample and the different layers can be appreciated. The thickness of the samples depended on the selected processing parameters. Figure 3b shows a detail of the cross-section of the sample shown in a). In addition, Fig. 4a shows the thickness of the fabricated samples depending on the different manufacturing conditions C1-C8 (Table 2). The influence of the laser power, scanning speed, and the carrying gas (argon or nitrogen) has been analyzed.

At low speed, the thickness of the samples increased with increasing power; at higher speeds, the width of the samples was smaller and remained uniform, except when N_2 was used, which caused a slight increase. On the one hand, this can be explained by considering that the higher the power, the higher the energy input. The Heat Energy Input depended on the laser power, and the scanning speed (Eq. 1).

$$\text{Heat Energy Input } \left(\text{J/mm}^3\right) = \frac{\textit{laser power } (W)}{\textit{scanning speed } \left({}^{mm}/_{s}\right)} \quad (1)$$

As in welding processes, the depth and width of the molten pool depend on the gas used, being greater when nitrogen was used due to its greater thermal conductivity. On the other hand, as the speed increased, the heat energy input and the amount of material deposited per unit of time decreased, which implies a decrease in the thickness.

The use of N_2 as a carrying gas induced higher thicknesses. Nitrogen gas (N_2) has a higher thermal conductivity than Ar, which caused more uniform heating of each deposited layer, favoring higher thicknesses. Furthermore, the high laser power may have generated the dissociation of the nitrogen molecules, inducing the exothermic reaction between nitrogen and the titanium molten particles that increased the temperature. The higher temperature reached increased the melting of the powder, increasing the powder deposition rates and, therefore, the thickness of the samples.

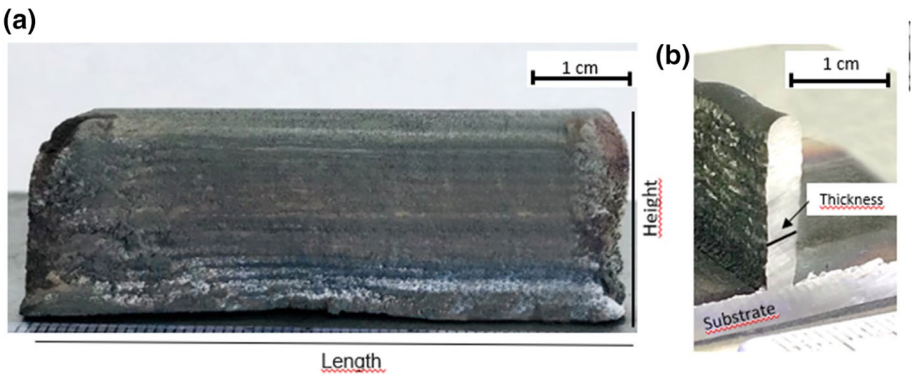

Fig. 3 **a** Macro-image of a DLD additively manufactured Ti/TiN sample; **b** cross-section of a sample shown in **a**

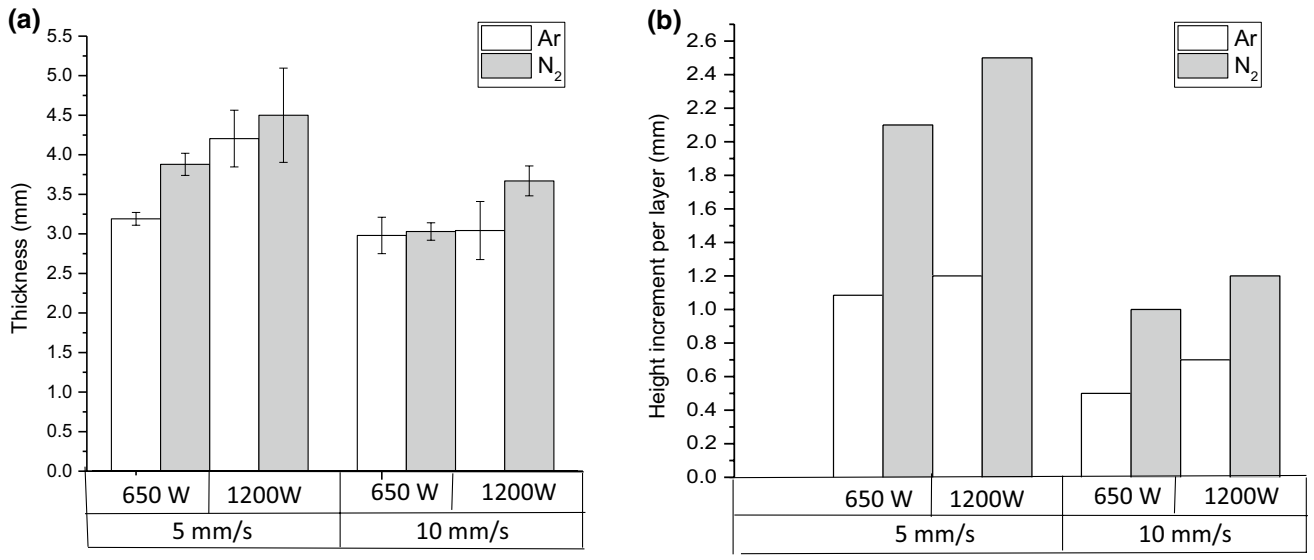

Fig. 4 **a** Thickness achieved for each scanning speed for each manufacturing condition (C1-C8) which varies the laser power, the scanning speed, and the carrying gas (argon or nitrogen); **b** Height increment per layer used for each manufacturing condition

The height increment per layer depended on the scanning speed, the laser power, and the carrying gas, as is plotted in Fig. 4b. The higher the scanning speed, the lower the height increment per layer needed to obtain the programed 15 mm height due to the lower heat energy input per layer. In the same way, the higher the laser power, the higher the height increment per layer. In addition, the selected carrying gas had a greater influence; the use of nitrogen as reactive gas increased the height of the layers due to the formation of TiN in the reaction between N_2 and titanium powders. Previous layers were less susceptible to heat remelting because the TiN meting point is much higher (2930 °C) than that of titanium (1668 °C), which explains the greater increases in height when using N_2 as a carrying gas,

The porosity percentage in the DLD samples is shown in Fig. 5 for the manufacturing conditions used (C1-C8), and variations with the laser scanning speed, the laser power, and the carrying gas were observed.

The porosity of the samples was below 2.5% for all the samples manufactured in the argon atmosphere, while the best value obtained with nitrogen was ~ 7%, going up to values of 27%. In all cases, porosity was higher for low laser energy values (650 W) for all manufacturing speeds. For high energy values (1200 W), porosity was lower, showing that the greater the fluidity of the molten metal the lower the porosity. The porosity of the samples manufactured with argon was very low and independent of the scanning speed. In the case of using nitrogen, the lower the scanning speed the greater the porosity.

Figure 6 shows the different defects that are formed. Figure 6a shows irregular defects observed in the 650-Ar-5 sample caused by the contraction of the metal during solidification (shrinkage cavities, marked with white arrows), with dimensions of between 40 and 80 µm in length; as well as some spherical pores caused by the trapping of gases (Fig. 6b) with diameters of ~ 25 µm. In the samples made with argon, zones with cracks due to a lack of melting were observed in the cross-section of the samples (Figs. 6 c-d) with sizes in the 200 to 600 µm range, and other authors have reported similar defects [32]. The appearance of these defects may be caused by insufficient melting of the material, but it may be also affected by the presence of residual stress after the manufacture of each layer, as the presence of stress may widen the defects during the cooling of each layer. However, these defects were not observed in the samples made with nitrogen because the higher thermal conductivity of nitrogen widens the molten pools.

Figure 6e shows the presence of defects in the 650-N-5 sample (arrowed) with lengths between 100 and 180 µm and also spherical shape porosity associated with trapped gas with diameters from 5 to 40 µm. These defects showed lack of melting, or lack of fluidity in the molten material. These effects can be explained by the presence of TiN formed in the solid phases in the molten Ti. It has been observed in different metal matrix composites [33, 34] that the presence of a solid phase in alloy increases the viscosity of the molten pool and limits the fluidity, increasing the number of defects.

Interdendritic porosity was observed (Fig. 6f), which was formed during the solidification process due to the contraction of the metal. The TiN dendrites were surrounded by liquid Ti6Al4V, so contraction occurred in the interdendritic spaces during solidification, giving rise to small cavities or pores measuring 1.06 ± 0.33 µm in length on average. This

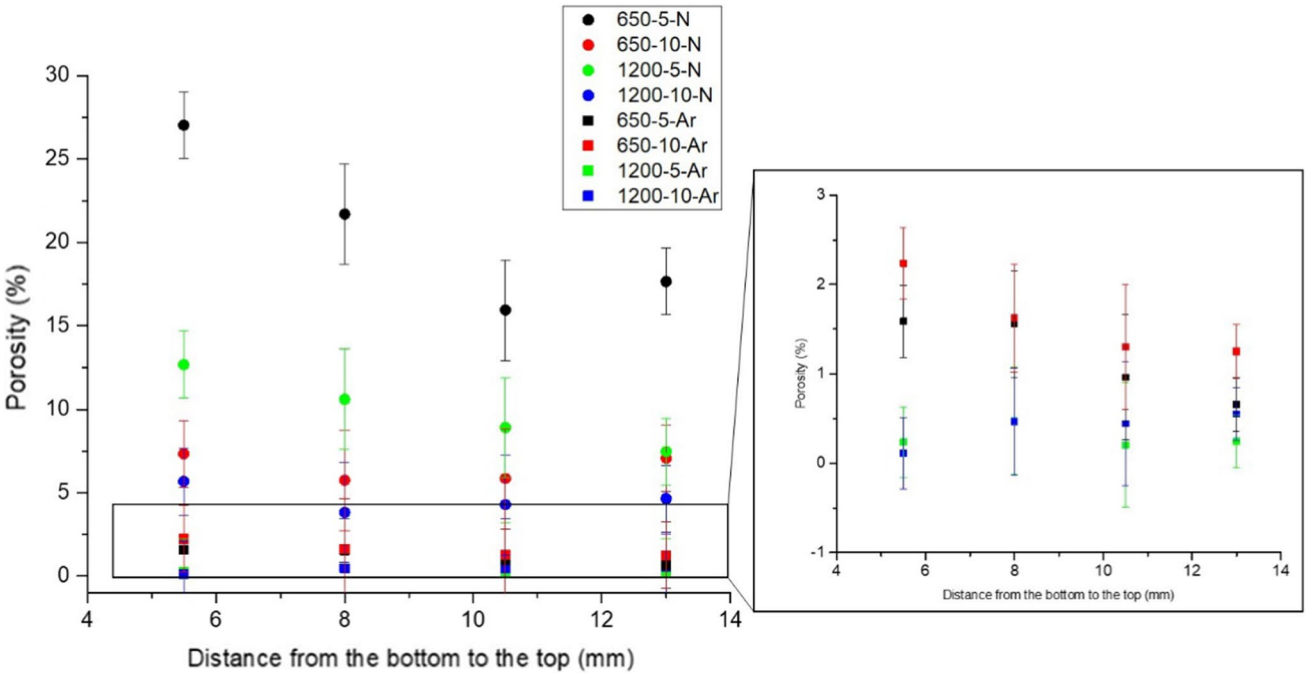

Fig. 5 Porosity percentage in the DLD samples for each manufacturing condition C1-C8; evolution of the porosity from the top to the bottom of the sample

type of porosity only appeared in the samples manufactured with nitrogen.

The differences in porosity are associated with the formation of TiN, which increases the viscosity of the molten pools because of the presence of a solid phase. During cooling, molten titanium solidifies but the high viscosity favors the formation of shrinkage cavities.

The effect of the laser scanning speed and the laser power on the microstructure of the DLD samples is shown in Fig. 7. Three cross-section images of each sample are exhibited to illustrate the microstructure at the top, middle, and bottom of the different samples. Microstructures formed using argon as carrying gas are shown in Fig. 7a, and Fig. 7b exhibits microstructures formed using nitrogen.

In the case of the samples manufactured with argon (Fig. 7a), a Widmanstätten alpha–beta titanium microstructure was identified. The alpha phase (α) corresponds to the elongated grains (dark grey thick plaques) and the beta phase (β) had an intergranular distribution (light grey fine plaques). Direct laser deposition causes high temperatures during manufacturing and relatively low cooling rates compared to other additive manufacturing processes such as Electron Beam Melting (EBM). Thus, the heat provided induces the decomposition of the α′ martensite to the equilibrium α + β microstructure [16].

No significant microstructural differences related to variations in the heat energy input were identified for the various manufacturing conditions. The heating during the manufacture of the subsequent layers hinders this effect. Small modifications took place at the bottom of the samples, which can be associated with the effect of conduction through the substrate, and no significant changes were observed in the microstructures of the upper zones of the samples.

In the samples manufactured using nitrogen (Fig. 7b), an alpha–beta titanium matrix and TiN dendrites are observed. The higher temperatures reached during the manufacturing process resulted in the reaction between the molten titanium and the nitrogen that formed TiN as dendrite compounds. The size and morphology of these dendrites depended on the processing parameters.

Higher scanning speed for the same laser power led to a decrease in the size of the dendrites due to the higher cooling rates and the lower heat energy input per layer. The most appreciable differences in the microstructure appeared in the central layers of the samples. In the lowest heat energy input condition (650–10-N), a morphology with dendrites forming circles was observed in the central zone of the samples. The different reaction mechanisms that influence the microstructure will be discussed later in the microstructural analysis section.

Figure 8 shows the X-ray diffraction spectra for the DLD samples fabricated with different laser conditions. When using argon as carrying gas (C1 to C4 conditions), the XRD peaks confirmed the presence of the alpha and beta phases, as well as TiN, although there were differences in the

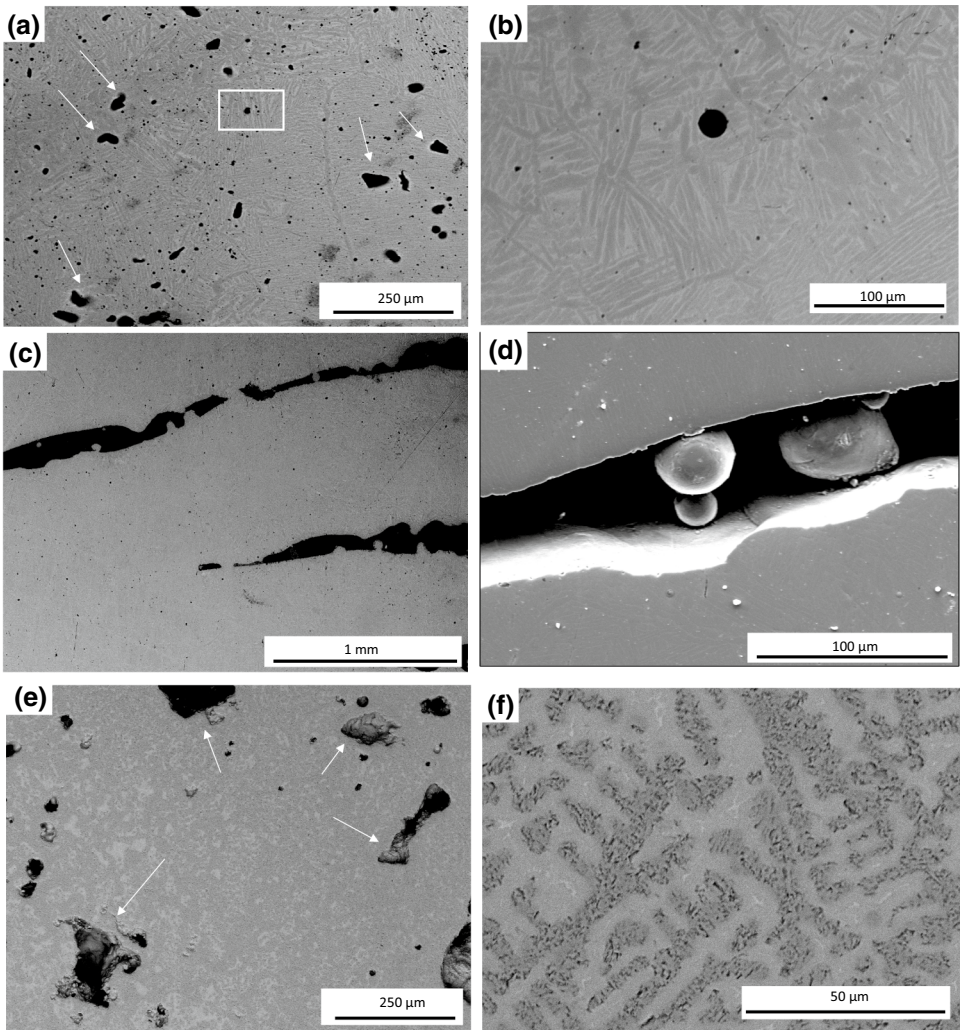

Fig. 6 BSE SEM Images of **a** porosity observed in the 650-5-Ar sample (C1 condition); **b** gas inclusion porosity in 650-10-Ar sample (C2 condition); **c** lack of melting in 1200-5-Ar sample (C3 condition); **d** high magnification detail of **c**; **e** porosity observed in the 650-5-N sample (C5 condition); **f** detail of the interdendritic porosity, high magnification detail of **e**

intensity of the alpha–beta peaks depending on the manufacture parameters.

For 650 W of laser power, the increment in the scanning speed from 5 mm/s to 10 mm/s, C1, and C2 conditions, respectively, resulted in a considerable decrease of the beta-titanium peak. The same occurred for conditions C3 and C4 that were manufactured with 1200 W of laser power. For each laser power value, the increment in the scanning speed led to a higher cooling rate, which restrained the decomposition of α′ martensite into the α + β phases.

When using nitrogen as reactive gas (C5 to C8 conditions), the α + β phases peaks height decreased and TiN and Ti_2N peaks appeared in the spectra, confirming the reaction between nitrogen and titanium. At low scanning speed (C5 and C7 conditions), increments in the laser power led to higher intensity of the TiN phases peaks. These peaks were similar in the samples fabricated at high scanning speed (C6 and C8 conditions), independently of the laser power. Ti_2N peaks intensity depended on the cooling rate, and Ti_2N was a minority phase. The formation of these phases also depended on the amount of nitrogen present during titanium solidification.

Wei W et al. [31] identified nitride precipitates in the XRD peaks, SEM, TEM images and EDS analysis of the characterization they performed on AM in-situ synthesized TiN reinforced Ti6Al4V matrix composites. The Ti6Al4V exhibited a Widmanstatten/basket-weave (α´) microstructure as a result of high cooling rate; and the composite materials microstructure presented a morphology of lath martensite with nanoscale granular nitride reinforcements uniformly dispersed (TiN).

Zhao X et al. [27] showed that the phase compositions of the in-situ textured TiN coatings they fabricated on TNZT titanium alloy were β-Ti, α´´ martensite, and TiN. They used a pulsed YAG:Nd laser with pulses of 0.3, 0.5, and 0.7 ms on a substrate manufactured by hot vacuum pressure sintering system. The distribution of the TiN dendrites was regulated by the reaction of the molten titanium with the nitrogen at high temperatures. The distribution, morphology, and size of the TiN depended on the processing conditions (laser

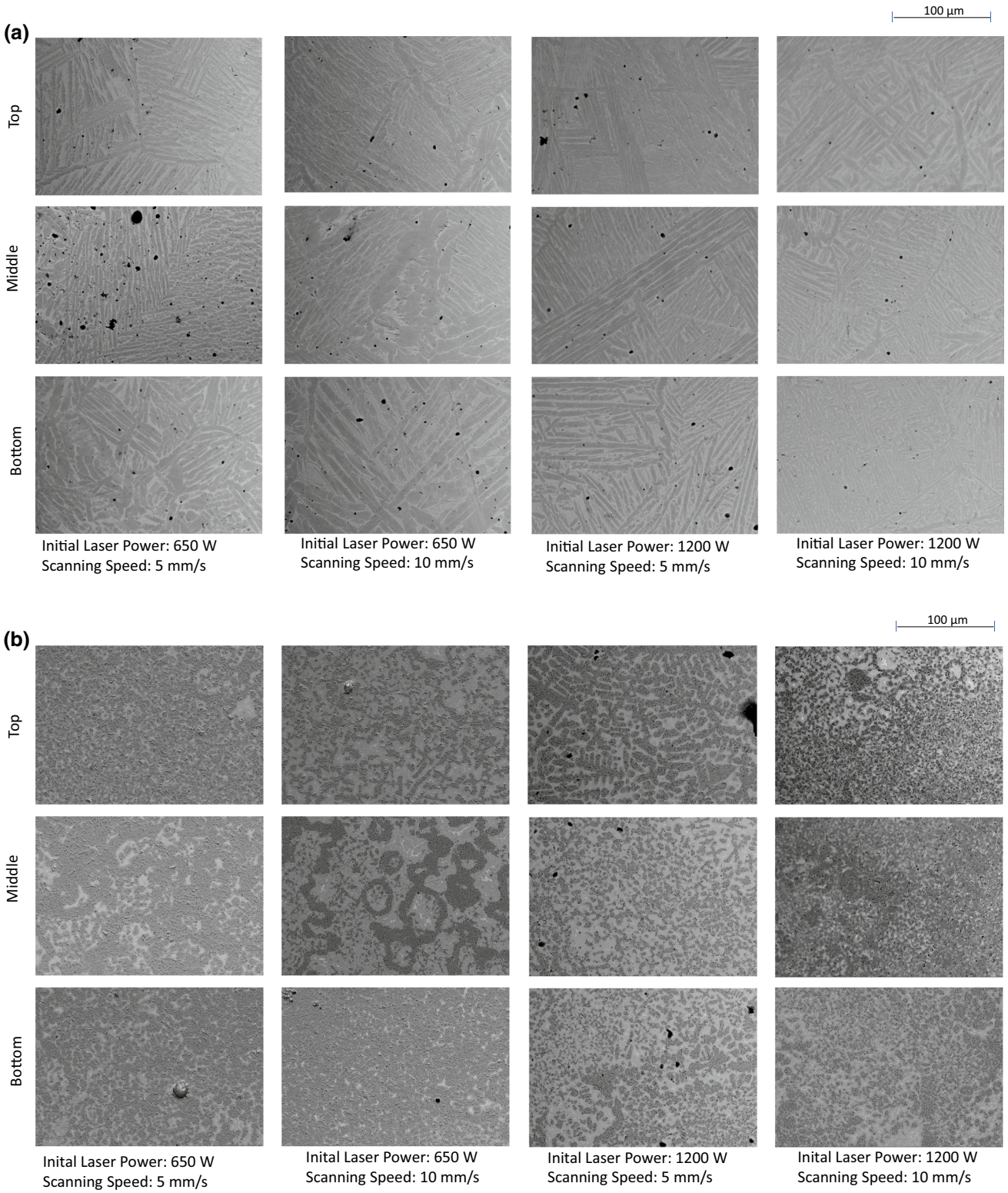

Fig. 7 Effect of the laser scanning speed on the microstructure of the samples. View of three cross-sections: top, middle, and bottom for each AM sample; **a** AM samples manufactured using argon as carrying gas; **b** AM samples manufactured using nitrogen as carrying gas

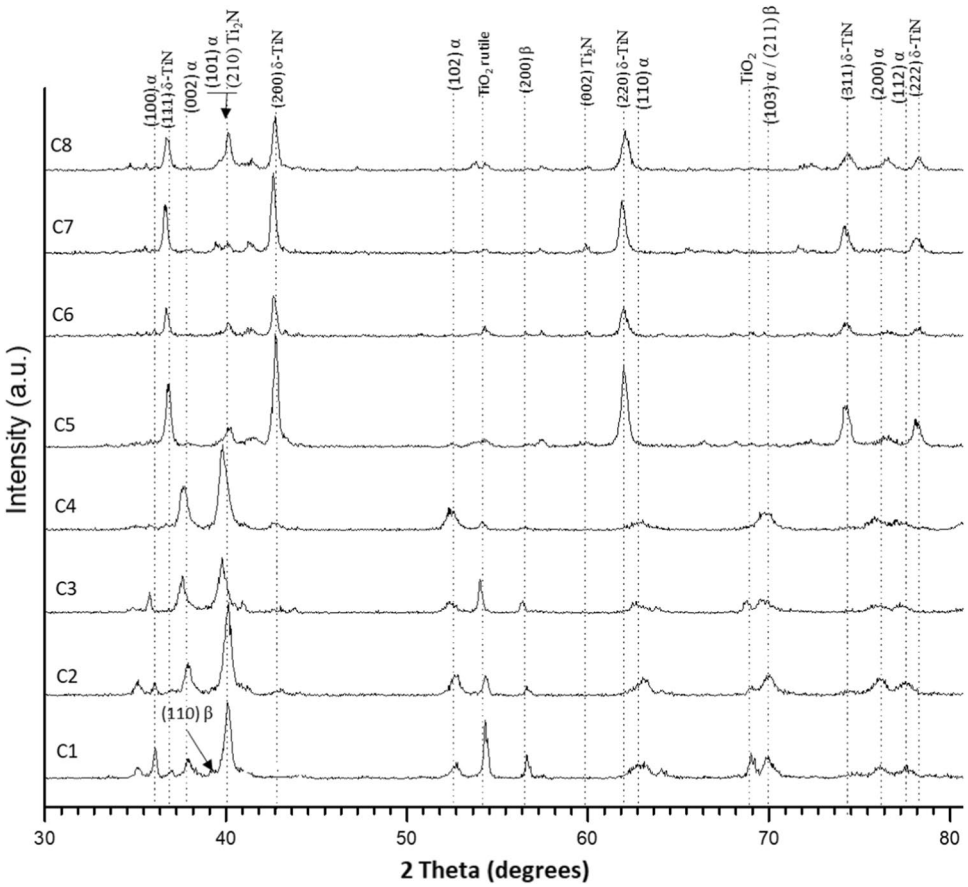

Fig. 8 X-ray diffraction profiles of DLD samples fabricated under C1–C8 conditions

pulse). The application of a pulsed laser increased by several orders of magnitude the cooling temperature of the treated surface giving rise to the formation of martensite, while for the lower cooling rates used in our work the structure was a Widemanstatten basket-weave.

The SEM images of the microstructure and the EDX elements map of the 650–5-N sample manufactured under C5 conditions (650 W, 5 mm/s, and nitrogen as carrying gas) are shown in Fig. 9. Figure 9a shows a general image of the microstructure and Fig. 9b shows a detail. In addition, the EDX elements maps made on the surface shown in Fig. 9b are displayed in Fig. 9c, where the different element-rich zones are shown.

The microstructure is formed by a titanium matrix in which an aluminum-rich zone (alpha phase) around the vanadium-rich zone (beta phase) can be appreciated. In addition, titanium nitride dendrites with high interdendritic porosity were observed (arrowed zones in Fig. 9b).

Figure 10 shows the microstructure of the 1200–5-N sample manufactured under C7 conditions (1200 W, 5 mm/s, and nitrogen as reactive gas). Figure 10a shows a general image of the microstructure, and its detail is shown in Fig. 10b. Figure 10c exhibits an elements analysis done in the marked zone of the microstructure, where the evolution of element-rich zones along the titanium matrix was analyzed.

As in the previous case, the microstructure was formed by a titanium matrix and titanium nitride dendrites. An aluminum-rich zone and a vanadium-rich one were present in the titanium matrix. The vanadium-rich zone was smaller than in the previous case, as can be observed in Fig. 8, where the beta-titanium phase peak is lower. For this condition, dendrites also showed higher porosity.

The microstructures were highly conditioned by the laser parameters used (heat energy input) and in consequence, the solidification and cooling rates were subject to the parameters of the fabrication process. Figure 11 shows the microstructure of two samples obtained with different laser parameters. The microstructure of the 650–10-N sample fabricated with the C6 condition (lower energy input) appears in Fig. 11a, and the microstructure of the 1200–5-N sample fabricated by C7 condition (greater heat energy input) is shown in Fig. 11b. Both images correspond to the central zone of the sample.

Circular patterns were observed in the microstructure of the sample manufactured with the lower input heat (Fig. 11a). The outer ring (zone 1) consisted of titanium nitride dendrites in a titanium matrix (TiN and eutectoid α-Ti -Ti_2N dendrites). Inside this ring, a thinner ring can be observed (zone 2) where the microstructure consisted of α-Ti phase matrix, TiN dendrites, and Ti_2N. Lastly, a third

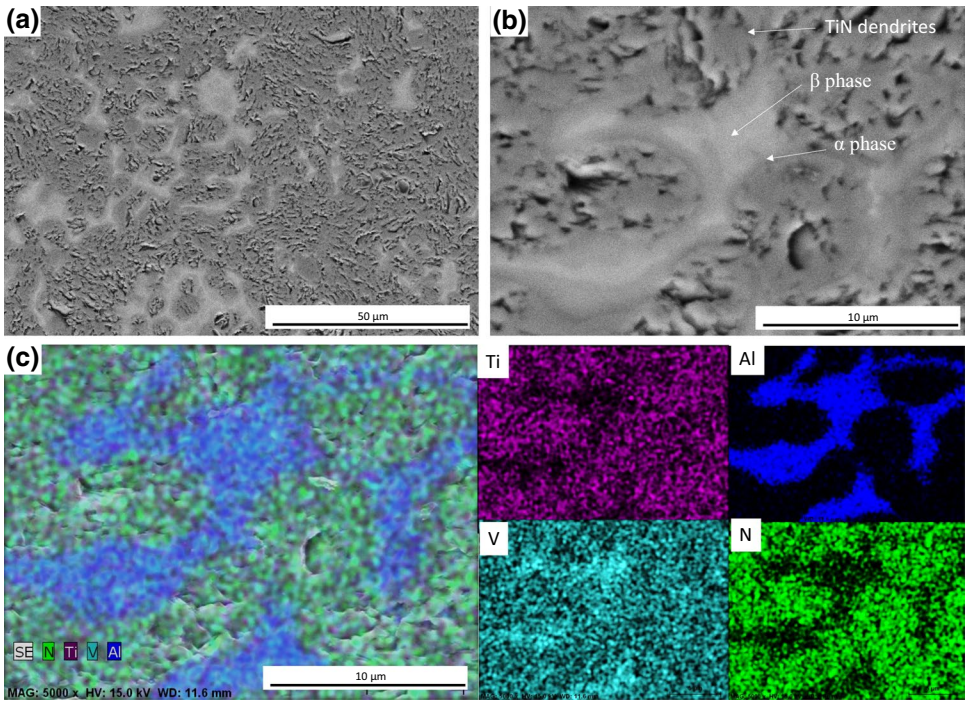

Fig. 9 Detail of the 650-5-N sample microstructure (C5 condition); **a** SEM image of the microstructure; **b** detail of **a**; **c** EDX elements map and SEM image

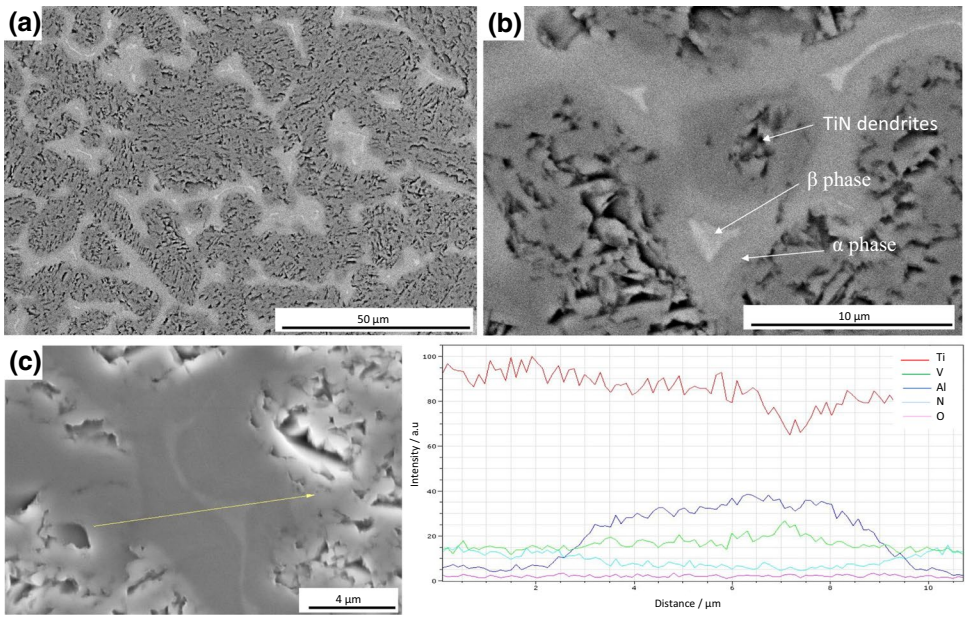

Fig. 10 Detail of the 1200-5-N sample microstructure fabricated using C7 condition; **a** SEM image, **b** high magnification of the matrix-dendrites interface; **c** elements analysis done in the marked zone

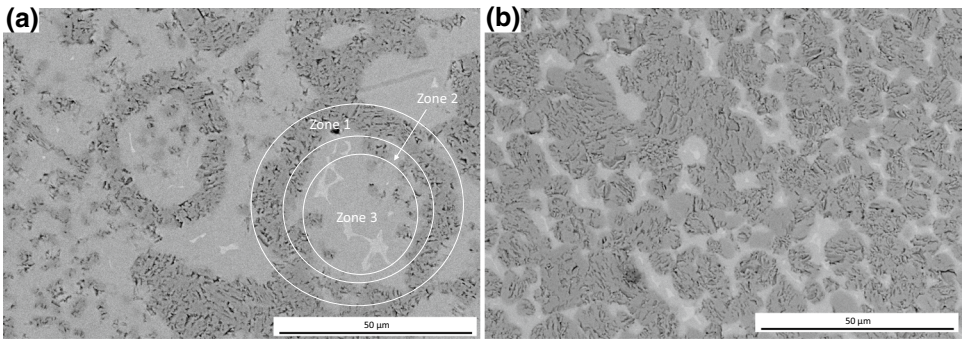

Fig. 11 **a** Microstructure of the 650-10-N sample fabricated with C6 condition; **b** microstructure of the 1200-5-N sample fabricated by C7 condition

ring was identified inside the other two: the titanium matrix microstructure which consists of primary dendrites of α-Ti phase and α + β phases (zone 3). Nitrogen reacted with the titanium and incorporated into the pieces. The amount of nitrogen (wt% nitrogen) was highest on the surface of the molten titanium particles and decreased from the surface to the inside the particle. Within the particles, the nitrogen atoms only propagate by diffusion, causing variations of the percentage of nitrogen across the molten titanium particles.

The geometry and size of these zones depended on the manufacturing parameters. These three zones were not observed for higher manufacturing energies (Fig. 11b) because the difussion of nitrogen into the titanium particles was favored, resulting in the growth of the dendrites.

Figure 12a represents schematically a titanium particle where three different zones can be appreciated as a function of the proportion of nitrogen. Depending on the amount of nitrogen, the reaction mechanism changes following the Ti-N phase diagram (Fig. 12b). Therefore, three different reaction mechanisms are proposed.

The first reaction mechanism occurs when the amount of nitrogen is higher than 7 wt%, the Ti-N system is located

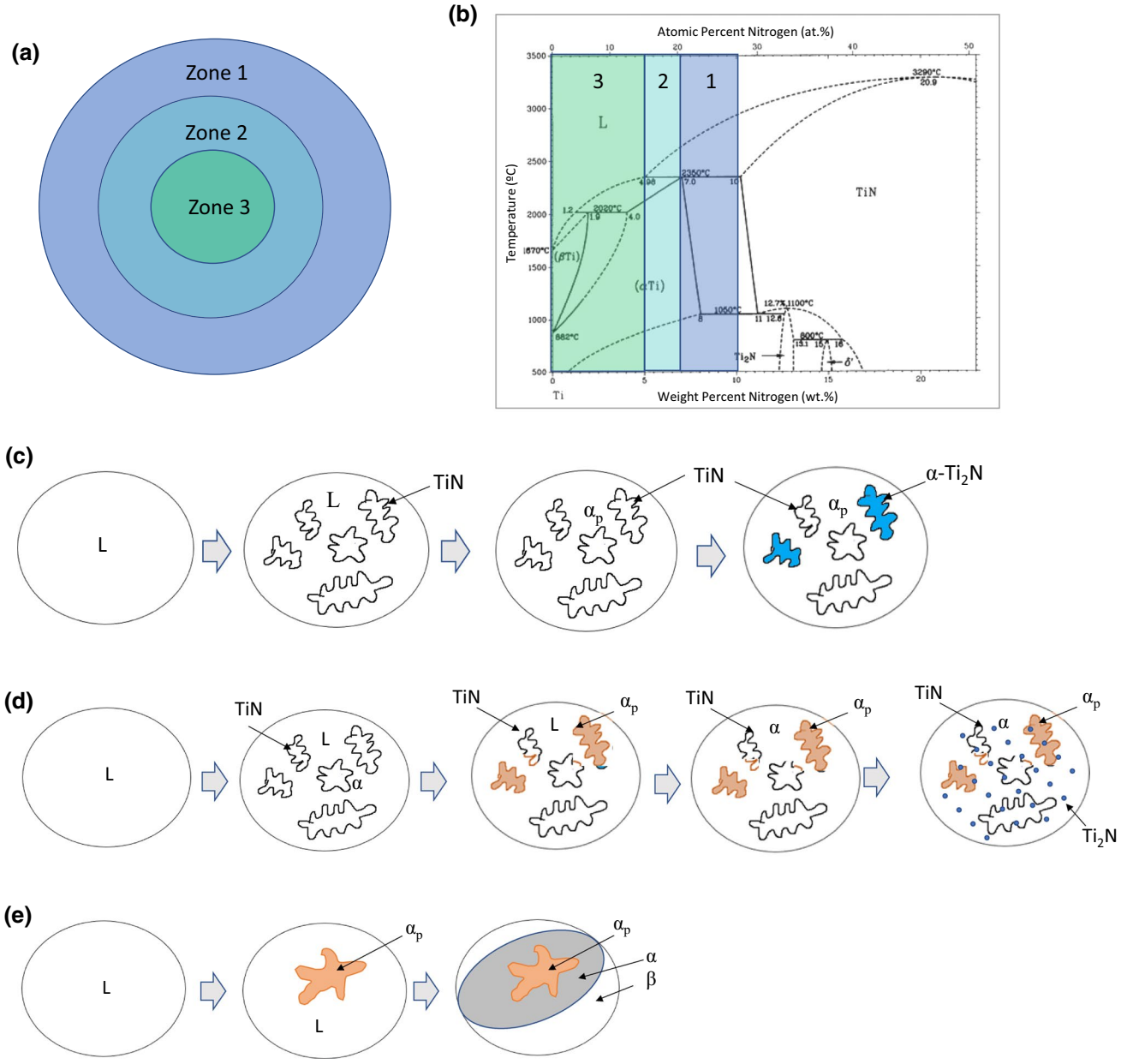

Fig. 12 **a** Scheme of the three different reaction mechanism zones; **b** Ti-N phase equilibrium diagram; **c** zone 1 reaction mechanism; **d** zone 2 reaction mechanism; **e** zone 3 reaction mechanism

at zone 1 in the phase diagram, and in it both, TiN and Ti saturated in N, can coexist. The reaction mechanism that takes place is schematically shown in Fig. 12c. First, the titanium particles are molten due to high temperatures, then the nitrogen from the atmosphere diffuses in the particle and reacts with the titanium and forms TiN dendrites. At 2350 °C, the α-Ti phase solidifies, and below 1050 °C some TiN dendrites suffer a transformation to eutectic α-Ti-Ti_2N. The resultant microstructure consists of an α-Ti phase matrix with dendrites of TiN and a eutectoid α-Ti -Ti_2N.

The second reaction mechanism takes place if the amount of nitrogen is between 5 wt% and 7 wt%, the Ti-N system is located at zone 2 in the phase diagram. In this zone, in the steady state only Ti with dissolved N should appear, but the kinetics of the reaction and the fast cooling made that part of the TiN remained. Figure 12d shows the reaction mechanism. The first stages are the same: first, the titanium particle is molten and reacts with the nitrogen forming TiN dendrites. Subsequently, primary α-Ti dendrites appear. Due to the higher cooling rates of the manufacturing process, not all of the TiN is dissolved, so some TiN is present in the final microstructure. The remaining molten titanium forms the α-Ti phase matrix and finally Ti_2N precipitates in the α-Ti matrix.

The last reaction mechanism occurs when the amount of nitrogen is below 5 wt%, which is located at zone 3 in the Ti-N phase diagram. Here, the first primary α-Ti phase dendrites form from the molten titanium and then the α + β Widmanstätten matrix forms (Fig. 12e).

The cooling rate depends on the laser fabrication parameters and also on the cooling through previously deposited layers. As a result, the three different reaction mechanisms can occur in the same sample.

Figure 13a shows a scheme of the microhardness measurements and Fig. 13b the Vickers microhardness evolution from the bottom to the top of each sample. Samples manufactured with nitrogen have a higher microhardness than those manufactured with argon. However, the deviation of the measurements on the samples fabricated using N_2 as carrying gas is rather high. This large variation along the sample is due to the phases that are formed during the manufacturing process resulting from the reaction between the nitrogen molecules and the titanium matrix. Although the microhardness was measured just for the metal matrix, these reinforcing phases are present in the whole sample and affect some measurements (they have a much higher Vickers microhardness compared to the titanium matrix); for instance, if they are formed in deeper layers of the materials, just underneath the Vickers indentation. This is quite common in metal matrix composites. In addition, these samples have greater porosity levels that affects the microhardness data. Nevertheless, the microhardness measured for samples manufactured with Ar as carrying gas is more homogeneous because it is a non-reinforced alloy which also present lower porosity levels. Furthermore, these changes in the microhardness may be also due to the variation in the microstructure from the bottom to the top of the sample.

Figure 13c shows the microhardness of the samples fabricated using the different conditions C1-C8 shown in Table 2 measured at the middle cross-section zone where the deviations of the microhardness measurements are lower. In all cases, the samples fabricated with nitrogen have higher microhardness values, which reached up to 100% more than those for the unreinforced materials.

Independently of the carrying gas used, an effect of the fabrication parameters in the microhardness can be observed. In all cases, the decrease of laser power increased the microhardness. However, the microhardness value tendency with the scanning speed depended on the carrying gas used.

The use of argon as carrying gas resulted in very similar microhardness values despite the scanning speeds used. Changes in this fabrication parameter did not affect the microhardness of the samples manufactured with argon. However, independently of the scanning speed used, an increase in the microhardness with the decrease of laser power can be observed, since the deposition of a layer causes annealing of the previously deposited layers at high laser power.

A connection between the resulting microstructures and the mechanical properties can be establish. When nitrogen was the reactive gas, the microhardness increased, which is related with the formation of TiN dendrites in the alpha–beta titanium matrix. The size and morphology of these dendrites depended on the laser power and the scanning speed and determined the microhardness measured. In this sense, for the composites with in-situ reinforcement, the higher the scanning speed, the lower the microhardness because the smaller reaction time between the nitrogen and the titanium gave rise to lower amounts of TiN in the composite with a decrease in the size of these dendrites.

Also, for the samples fabricated with nitrogen, an important increment in the microhardness with the decrease of laser power (an increment between 15 and 25%) was observed because at low laser power the annealing of the microstructure was avoided. This composite has high porosity, and its effect can be observed in the abrupt changes in the microhardness measured, but these values are less affected by the presence local defects than other mechanical properties.

Finally, the variation in the microhardness along the sample depends on the different phases that are formed. For instance, the most appreciable changes in the microstructure appeared in the central layers of the samples (Fig. 7b).

Wei et al. [31] manufactured Ti/TiN samples by Selective Laser Melting (SLM) with 400–511 HV. In this research the microhardness of the manufactured samples

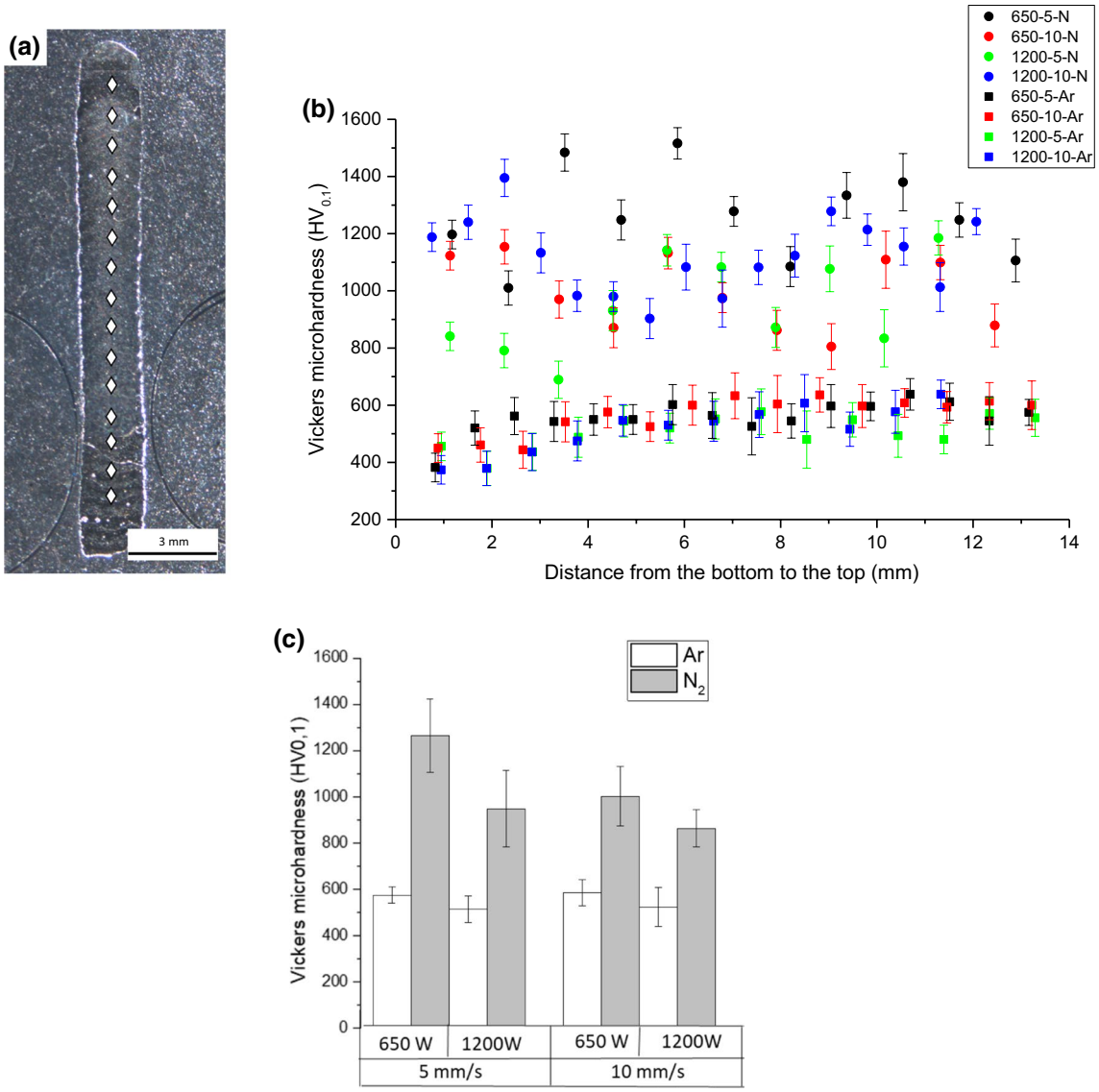

Fig. 13 **a** Scheme of the microhardness measurements; **b** Vickers microhardness evolution from the bottom to the top of the sample; **c** Microhardness values of the samples fabricated with different conditions (C1-C8)

was between 800 and 1200 HV. Cui et al. [33] obtained higher microhardness, however they manufactured coatings on Ti6Al4V substrates.

4 Conclusions

The additive manufacturing of highly hardening titanium metal matrix composites reinforced with in situ titanium nitride by direct metal deposition has been satisfactorily obtained, and the influence of the carrying gas and process parameters have been determined, as follows:

- Higher scanning speeds and lower laser powers resulted in layers with lower thickness, less height, and less porosity as a result of smaller net energy input.
- The use of nitrogen gas resulted in thicker and higher layers with greater porosity, and its reaction with the molten titanium particles led to an in situ titanium matrix composite highly reinforced with TiN.
- A Widmanstätten alpha–beta titanium matrix was obtained when using argon as carrying gas, while an alpha–beta titanium matrix and dendrites formed by titanium and nitrogen were observed when using nitrogen.

- Three reaction mechanisms have been proposed depending on the wt% of nitrogen in the titanium particles introduced by diffusion during the manufacturing process.
- The use of nitrogen resulted in microhardness increments between 50 and 100%. At low laser power, the annealing of the microstructure was avoided and an increase of 25–15% in the microhardness was measured.

Supplementary Information The online version contains supplementary material available at https://doi.org/10.1007/s12540-022-01260-2.

Acknowledgements This work was supported by Comunidad de Madrid (ADITIMAT-CM S2018/NMT-4411) and ADITINANO (2020/00007/019).

Funding Open Access funding provided thanks to the CRUE-CSIC agreement with Springer Nature. Authors reports financial support was provided by Universidad Rey Juan Carlos and Comunidad de Madrid.

Declarations

Conflict of interest The authors declare that they have no known competing financial interests or personal relationships that could have appeared to influence the work reported in this paper.

References

1. G. Rasiya, A. Shukla, K. Saran, Mater. Today Proc. **47**, 6896 (2021). https://doi.org/10.1016/j.matpr.2021.05.181
2. C.T. Lynch, J.P. Kershaw, *Metal Matrix Composites* (CRC Press, Boca Raton, 1972). https://doi.org/10.1201/9781351074445
3. A. Bhatia, A.K. Sehgal, Mater. Today Proc. (2021). https://doi.org/10.1016/j.matpr.2021.04.379
4. C. Selcuk, Powder Metall. **54**, 94 (2011). https://doi.org/10.1179/174329011X12977874589924
5. C. Zhong, J. Liu, T. Zhao, T. Schopphoven, J. Fu, A. Gasser, J.H. Schleifenbaum, Appl. Sci. **10**, 764 (2020). https://doi.org/10.3390/app10030764
6. N. Shamsaei, A. Yadollahi, L. Bian, S.M. Thompson, Addit. Manuf. **8**, 12 (2015). https://doi.org/10.1016/j.addma.2015.07.002
7. J. Liang, Z. Lin, X. Yin, S. Chen, C. Liu, R. Chai, H. Zhang, G. Tang, K. Tian, Met. Mater. Int. **28**, 216 (2022). https://doi.org/10.1007/s12540-021-01035-1
8. R.M. Mahamood, E.T. Akinlabi, Mater. Today Proc. **5**, 18362 (2018). https://doi.org/10.1016/j.matpr.2018.06.175
9. A. Riquelme, P. Rodrigo, M.D.D. Escalera-Rodriguez, J. Rams, J. Manuf. Process. **46**, 271 (2019). https://doi.org/10.1016/j.jmapro.2019.09.011
10. S.M. Thompson, L. Bian, N. Shamsaei, A. Yadollahi, Addit. Manuf. **8**, 36 (2015). https://doi.org/10.1016/j.addma.2015.07.001.
11. A. Aversa, A. Saboori, E. Librera, M. de Chirico, S. Biamino, M. Lombardi, P. Fino, Addit. Manuf. **34**, 101274 (2020). https://doi.org/10.1016/j.addma.2020.101274
12. C. Zeng, H. Wen, H. Bellamy, P.T. Sprunger, P.J. Schilling, S.M. Guo, Surf. Coat. Tech. **378**, 124955 (2019). https://doi.org/10.1016/j.surfcoat.2019.124955
13. J. Abenojar, F. Velasco, A. Bautista, M. Campos, J.A. Bas, J.M. Torralba, Compos. Sci. Technol. **63**, 69 (2003). https://doi.org/10.1016/S0266-3538(02)00179-3
14. D. Herzog, V. Seyda, E. Wycisk, C. Emmelmann, Acta Mater. **117**, 371 (2016). https://doi.org/10.1016/j.actamat.2016.07.019
15. J. Zhu, H. Zhou, C. Wang, L. Zhou, S. Yuan, W. Zhang, Chinese J. Aeronaut. **34**, 91 (2021). https://doi.org/10.1016/j.cja.2020.09.020
16. S. Liu, Y.C. Shin, Mater. Design **164**, 107552 (2019). https://doi.org/10.1016/j.matdes.2018.107552
17. L.S. Wickramaratne, Risk analysis of Ti6Al4V Fasteners failures in aircraft and aerospace industries Lahiru Sajith Wickramaratne (19867871), Technical Report (2019). https://doi.org/10.13140/RG.2.2.20833.66404.
18. T. Bhardwaj, M. Shukla, N.K. Prasad, C.P. Paul, K.S. Bindra, Met. Mater. Int. **26**, 1015 (2020). https://doi.org/10.1007/s12540-019-00464-3
19. C.-W. Chan, J. Quinn, I. Hussain, L. Carson, G.C. Smith, S. Lee, Surf. Coat. Tech. **405**, 126714 (2021). https://doi.org/10.1016/j.surfcoat.2020.126714
20. J.D. Avila, K. Stenberg, S. Bose, A. Bandyopadhyay, Acta Biomater. **123**, 379 (2021). https://doi.org/10.1016/j.actbio.2020.12.060
21. S. Yuan, N. Lin, J. Zou, X. Lin, Z. Liu, Y. Yu, Z. Wang, Q. Zeng, W. Chen, L. Tian, L. Qin, R. Xie, B. Li, H. Zhang, Z. Wang, B. Tang, Y. Wu, Vacuum **176**, 109327 (2020). https://doi.org/10.1016/j.vacuum.2020.109327
22. J. Li, B.Y. Zong, Y.M. Wang, W.B. Zhuang, Mater. Sci. Eng. A **527**, 7545 (2010). https://doi.org/10.1016/j.msea.2010.08.029
23. M. Iorio, F. Marra, M.L. Santarelli, J. González-Benito, Constr. Build. Mater. **309**, 125103 (2021). https://doi.org/10.1016/j.conbuildmat.2021.125103
24. H. Attar, S. Ehtemam-Haghighi, D. Kent, M.S. Dargusch, Int. J. Mach. Tools Manuf. **133**, 85 (2018). https://doi.org/10.1016/j.ijmachtools.2018.06.003
25. G. Qiao, B. Zhang, Q. Bai, Y. Gao, W. Du, Y. Zhang, J. Manuf. Process. **76**, 412 (2022). https://doi.org/10.1016/j.jmapro.2022.02.033
26. P. Rodrigo Herrero, A. Riquelme Aguado, M.D. Escalera Rodríguez, J. Rams Ramos, Spain Patent, ES2598727B2 (2015)
27. B. Shi, S. Huang, P. Zhu, C. Xu, P. Guo, Y. Fu, Mater. Lett. **276**, 128093 (2020). https://doi.org/10.1016/j.matlet.2020.128093
28. C. Song, M. Liu, Z.-Q. Deng, S.-P. Niu, C.-M. Deng, H.-L. Liao, Mater. Lett. **217**, 127 (2018). https://doi.org/10.1016/j.matlet.2018.01.068
29. X. Zhao, P. Zhang, X. Wang, Y. Chen, H. Liu, L. Chen, Y. Sheng, W. Li, J. Mech. Behav. Biomed. Mater. **78**, 143 (2018). https://doi.org/10.1016/j.jmbbm.2017.11.019
30. K.D. Traxel, A. Bandyopadhyay, Addit. Manuf. **31**, 101004 (2020). https://doi.org/10.1016/j.addma.2019.101004
31. W. Wei, W. Wu, S. Fan, X. Duan, Mater. Design **202**, 109578 (2021). https://doi.org/10.1016/j.matdes.2021.109578

32. P.-H. Li, W.-G. Guo, W.-D. Huang, Y. Su, X. Lin, K.-B. Yuan, Mater. Sci. Eng. A **647**, 34 (2015). https://doi.org/10.1016/j.msea.2015.08.043
33. A. Mostafaei, C. Zhao, Y. He, S.R. Ghiaasiaan, B. Shi, S. Shao, N. Shamsaei, Z. Wu, N. Kouraytem, T. Sun, J. Pauza, J.V. Gordon, B. Webler, N.D. Parab, M. Asherloo, Q. Guo, L. Chen, A.D. Rollett, Curr. Opin. Solid State And Mater. Sci. **26**, 100974 (2022). https://doi.org/10.1016/j.cossms.2021.100974.
34. S.A. Sajjadi, M.T. Parizi, H.R. Ezatpour, A. Sedghi, J. Alloy. Compd. **511**, 226 (2012). https://doi.org/10.1016/j.jallcom.2011.08.105